Aeolian Research 13 (2014) 35–50

Contents lists available at ScienceDirect

Aeolian Research

journal homepage: www.elsevier.com/locate/aeolia

Accounting for surface roughness on measurements conducted with PI-SWERL: Evaluation of a subjective visual approach and a photogrammetric technique

V. Etyemezian [a,*], J.A. Gillies [a], M. Shinoda [b], G. Nikolich [a], J. King [c], A.R. Bardis [a]

[a] Division of Atmospheric Sciences, Desert Research Institute, Las Vegas and Reno, NV, USA
[b] Arid Lands Research Center, Tottori University, Tottori, Japan
[c] Department of Geography, Indiana University, Bloomington, IN

ARTICLE INFO

Article history:
Received 21 November 2012
Revised 4 February 2014
Accepted 3 March 2014
Available online 14 April 2014

Keywords:
Photogrammetry
Wind tunnel
PI-SWERL
Dust emission
Sand transport

ABSTRACT

The effect of small-scale surface roughness on measurements with PI-SWERL (The Portable In-Situ Wind Erosion Laboratory) was investigated using a viscometer-type device. The relationship between shear stress at the soil surface and PI-SWERL rate of rotation (RPM) was determined empirically with test surfaces of varying roughness including fine to coarse sandpaper, small domed structures (H = 2.5–2.9 mm) arranged in arrays, small ($H \approx 2$ mm) and large pebbles ($H \approx 5$–7 mm), thin cylinders representing blades of grass ($D \approx 2$ mm), and wave-like surfaces intended to represent small ripples. An empirical equation that uses a single parameter α was developed to relate RPM to the shear stress experienced by a test surface. Two methods were presented for estimating α. The first relies on a user's ability to estimate α by comparing to a catalog of standards of roughness. The second uses a digital photogrammetry technique in combination with image processing to parameterize roughness. The photographic method offers a factor of two improvement in estimation of α compared to the first method. Although a limited number of surfaces was tested, the photogrammetry technique appears to warrant further development. Additional findings relate to the optimal effective area for use in calculating wind erosion parameters from field tests and an estimate of errors for both dust emissions measurements and the associated friction velocity (u_*) when using the PI-SWERL. Overall, this work serves to reduce the uncertainties associated with using the PI-SWERL as a tool for estimating windblown dust emissions.

1. Introduction

The Portable In-Situ Wind Erosion Laboratory (PI-SWERL) (Etyemezian et al., 2007) has become an important instrument that is used by researchers to characterize and quantify dust emission potential for natural surfaces, both in disturbed and undisturbed conditions (Sweeney et al., 2008, 2011), and surfaces that emit dust that have been formed by human activities (e.g., exposed shorelines of the Salton Sea, CA (King et al., 2011), Williston Reservoir, B.C. (Nickling et al., 2011)). This compact instrument creates a shear stress (τ) on the surface of interest using a rotating annular blade positioned ≈0.05 m above the surface and in a sealed container with a flow-controlled exhaust port. The dust and sand entrained by the τ are measured using optically based instruments that measure light scattering from the suspended dust (e.g., TSI, Inc., DustTrak Models 8520, or 8530) and sand grain movement using multiple optical gate sensors. Prior to the research presented here τ was estimated based on a calibration relationship presented in Etyemezian et al. (2007) that relates τ (or friction velocity, u_*) with revolutions per minute (RPM) of the annular blade developed for a smooth, flat surface. The roughness of a surface however, is well-known to affect the magnitude of τ developed by the boundary-layer flow. Hence the application of the calibration relationship of Etyemezian et al. (2007) for a range of surface roughness is not ideal.

To overcome this limitation and to allow PI-SWERL users to better estimate τ generated by the rotating annular blade, a detailed set of experiments was undertaken to establish how roughness elements of different scales and distributions affect τ and to establish a relationship between roughness and the effective shear stress (τ_{eff} or $u_{*,eff}$) as a function of blade RPM. This was accomplished using a device that is similar to a viscometer in its principal of operation to infer τ on a test surface. From the experiments carried

* Corresponding author. Address: Division of Atmospheric Sciences, DRI, 755 E. Flamingo Road, Las Vegas, NV 89119, USA. Tel.: +1 (702) 862 5569; fax: +1 (702) 862 5507.
E-mail address: vic@dri.edu (V. Etyemezian).

http://dx.doi.org/10.1016/j.aeolia.2014.03.002
1875-9637/

out we are able to link surface roughness with its effect on τ_{eff} (or $u_{*,eff}$) using a simple visual test or for increased accuracy, a camera-based roughness measurement and image processing algorithm can be used.

2. Background

The role of surface roughness on the magnitude of τ in boundary-layer flow (e.g., Nikuradse, 1933; Colebrook, 1939; Lettau, 1969; Flack and Schultz, 2010) and the partitioning of that stress as affected by the distribution and size of the roughness (e.g., Schlichting and Gersten, 2000; Wooding et al., 1973; Raupach, 1992; Raupach et al., 1993, 2006; Brown et al., 2008; Shao and Yang, 2008) have been rich areas of research in fluid mechanics and wind erosion (e.g., Chepil, 1950; Gillies et al., 2006, 2007). The physical size and distribution of roughness has a profound effect on the boundary-layer. Following Prandtl (1925), τ can be shown to be constant across the turbulent boundary-layer, and by integrating the vertical velocity profile that increases logarithmically with height (z) the "law of the wall" is derived:

$$U_z = \frac{U_*}{\kappa} \ln \frac{z}{z_0} \quad (1)$$

where u_z [m/s] is fluid speed at height z [m], u_* is shear or friction velocity ($\tau = \rho u_*^2$) [m/s], κ is von Kármán's constant (0.4), and z_0 is the aero/hydrodynamic roughness length [m]. z_0 is a constant of integration and relates to the physical roughness of the surface. It is the height above the surface where the velocity would be zero when extrapolating the logarithmic profile.

For physically smooth surfaces a viscous sub-layer forms and the matching of the logarithmic profile between the inner and outer layers determine the value of z_0. If the physical roughness of the surface is larger than the viscous sub-layer, turbulent mixing dominates the flow near the bed and the mixing length L (Prandtl, 1925) is controlled by the roughness. Under these conditions z_0 shows dependence on the roughness and independence from the fluid speed (and Reynolds number). For surfaces composed of fixed granular material of diameter d [mm], the estimated value of z_0 has been shown to scale reasonably consistently as $z_0 = d/30$ (Bagnold, 1941), and $z_0 = d/24$ (Schlichting and Gersten, 2000). When roughness is non-uniform it has been defined as the root mean square of the height (RMS height) profile variations (e.g., Greeley et al., 1991), but the relationship between z_0 and RMS height is not well-established as roughness parameters such as roughness form may also influence z_0 (Dong et al., 2002). As Flack and Schultz (2010) demonstrate, no single roughness height parameter (e.g., RMS height, equivalent sand grain height k_s (Nikuradse, 1933)) is able to collapse roughness function results in all flow regimes for a range of surface roughness (see Figs. 3 and 4).

Although relating specific roughness parameters to aerodynamic roughness length remains an area of active research, there have been some helpful developments in the quantifying of roughness parameters. Notably, Chappell et al. (2010) examined the data of Dong et al. (2002) as well as that of Marshall (1971) to evaluate angular reflectance of rough surfaces as a means to quantify the effect of roughness on wind erosion. Chappell et al. (2010) reasoned that the area corresponding to the shadow of a surface that is illuminated from an oblique angle can be used to infer the aerodynamic roughness of that surface. They reconstructed shadows of the roughness arrays used by Dong et al. (2002) and Marshall (1971) over a range of illumination zenith angles (measured from the line that is perpendicular to the surface) as well as azimuth angles (measured in the plane parallel to the surface from some arbitrary datum). The dependence of the shadow on these two illumination angles was removed by integrating over all illumination angles and calculating a single parameter the authors termed a Single Scattering Albedo (SSA) for the surface of interest. Integration over the azimuth angle served to include the effects of anisotropy in the roughness element arrangement whereas integrating over the zenith angles was used to ameliorate the impact of roughness elements casting shadows on (hiding) other roughness elements. Chappell et al. (2010) then related SSA to the ratio of aerodynamic roughness to physical roughness height (z_0/h) for the data of Dong et al. (2002) using a Gaussian model. The data of Marshall (1971) were considered less representative of natural roughness elements since Marshall (1971) used sharp-edged blocks for roughness; Dong et al. (2002) used hemispheroids, which Chappell et al. (2010) reasoned are likely more representative of field scale roughness element shapes. The Gaussian fit was then applied to a natural surface that had both digital elevation information (DEM) and aerodynamic roughness measurements (z_0). Chappell et al. (2010) found that the Gaussian model did not appear to replicate the directional dependence of the observed z_0 values, but did provide good agreement with the directionally averaged z_0.

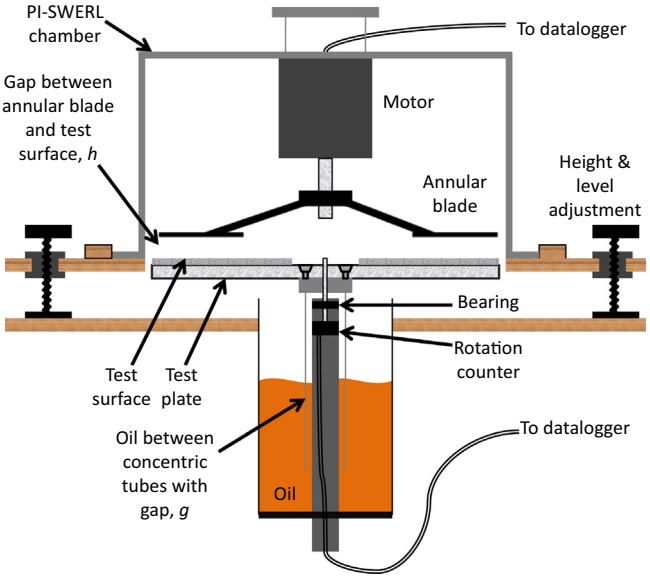

Fig. 1. Experimental setup for measuring shear-stress.

Recent advances in photographic and laser-imaging methods have enabled the economical use of these techniques to characterize and parameterize surface roughness and examine their effects on wind and water erosion. Kirby (1991) used advanced photographic techniques to obtain stereo images of desert terrain roughness. Lane et al. (2000) and Jester and Klik (2005) discuss the applications of photogrammetry and other roughness measurement techniques in surface characterization. Laser retrieval techniques, namely LiDAR (Light Detection and Ranging) have also been used to obtain surface roughness and digital elevation contours over varying scales of surfaces pertinent to water and wind erosion (e.g., Hodge et al., 2009; Sankey et al., 2011; Nield et al., 2013). Moreover, the same technique can also be used to map vegetation distribution and properties (e.g., Eitel et al., 2010; Sankey et al., 2010), making it a scalable tool for field studies. Aguilar et al. (2009) compared photogrammetric techniques with laser-based methods and found that laser methods provided slightly better resolution but that both methods were able to resolve sub-millimeter features. The excellent resolution provided by commercial digital cameras along with the relatively low cost, render photogrammetry an attractive choice in many practical applications.

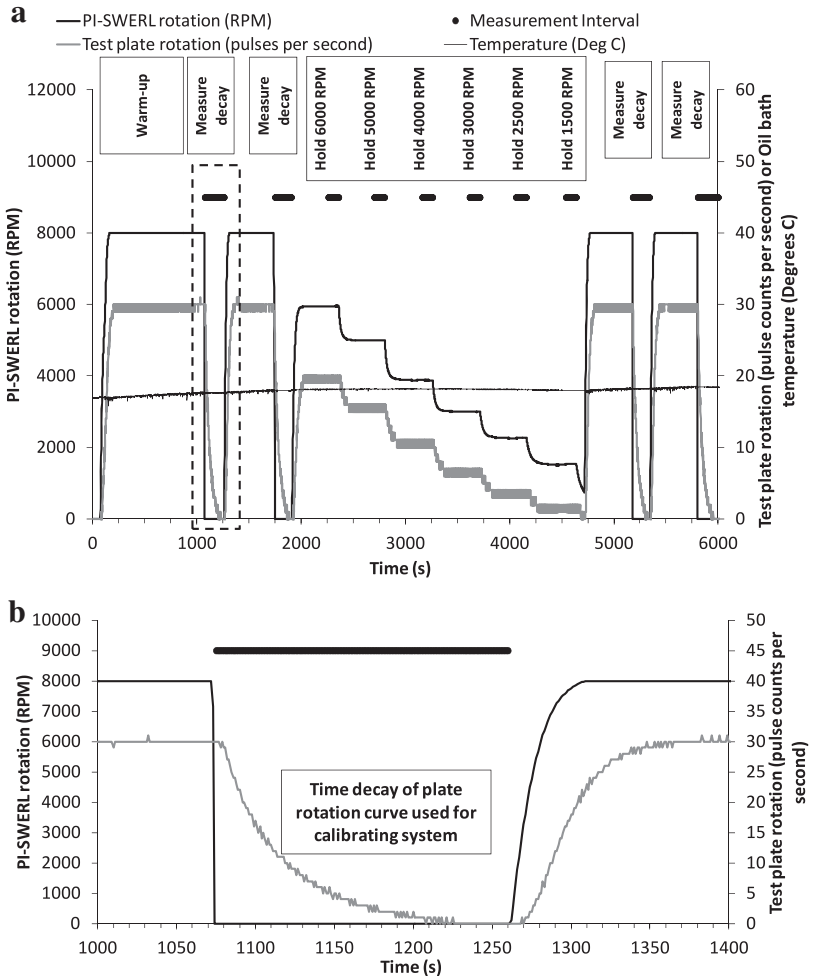

Fig. 2. Example of RPM test cycle. Thick black lines correspond to periods when measured values are used during data processing. (a) example RPM curve test cycle and (b) expanded scale corresponding to dashed box in a.

3. Methods

The PI-SWERL and the miniature version used in the present work have been described in detail by other authors (e.g., Etyemezian et al., 2007; Sweeney et al., 2008, Kavouras et al., 2009; Goossens and Buck, 2009). We therefore provide only a brief overview here. The miniature PI-SWERL is a cylindrical chamber (diameter, D = 0.30 m; height, H = 0.20 m) that is open at the bottom and closed at the top except for an exhaust port. An annular blade (outer diameter, OD = 0.254 m; inner diameter, ID = 0.178 m) is centered horizontally within the chamber and is held in place by a shaft coupling to a direct current (DC) motor that is fastened to the top of the chamber. The annular blade is attached to a collar that can slide along the motor shaft to vary the distance between the blade and the test surface if desired. In practice, a set screw is used to fix the blade so that the bottom of the blade is 0.045 m from the bottom of the PI-SWERL chamber – defined as the bottom surface of the aluminum flange (including the orange, silicon material that is used for gluing the flexible foam). The height of the annular blade is usually not intentionally varied in the field. Flexible, compressible foam is attached along the perimeter of the bottom of the PI-SWERL. This foam accommodates small irregularities on the test surface and serves as a seal between the chamber and the surface. Although in its uncompressed state, the foam is 0.05 m thick, it easily compresses to between 0.007 and 0.025 m under the weight of the PI-SWERL. The degree of compression depends on the age of the foam, the slope of the surface, and the types of roughness the foam is accommodating. Thus, when in use in the field, the distance between the PI-SWERL blade and the test surface is somewhat difficult to quantify with certainty. It can range between 0.052 and 0.070 m. However, in the experience of the authors, a typical compressed thickness for the foam is 0.009–0.020 m and accordingly typical blade to test surface distances are 0.054–0.065 m.

In earlier work (Etyemezian et al., 2007; Kavouras et al., 2009), the empirical relationship between the rate of rotation of the annular blade and the amount of shear stress induced on the test surface was estimated for smooth test surfaces using Irwin sensors, which were used to relate pressure gradients within the boundary layer close to the test surface to the shear stress. In the current work, a device that is similar to a rotational viscometer was used to quantify the equivalent friction velocities experienced by a surface undergoing a PI-SWERL test. A viscometer is used to measure the viscosity of a fluid. There are numerous configurations for such a device, but in a rotational viscometer, the fluid whose viscosity is to be measured is placed between two concentric surfaces such as cylinders. One cylinder is spun relative to the other at a specified rate of rotation. The amount of torque needed to maintain this rotation is measured and can be related through basic principles of fluid mechanics to the gap between the two concentric surfaces, rate of rotation, and the viscosity of the fluid of interest.

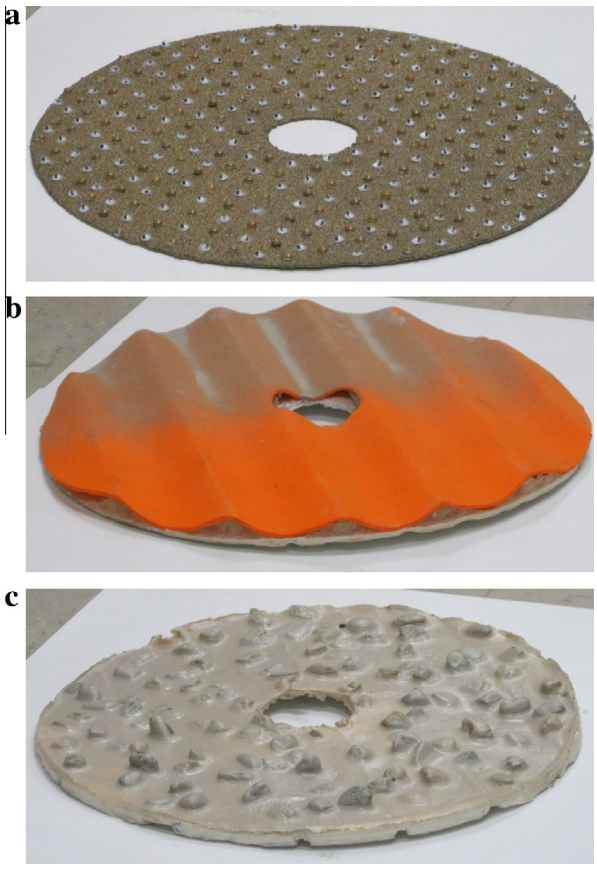

Fig. 3. Examples of test surfaces. (a) Small domes on #36 sand paper (SP-36_GES-AEMUY), with half of domes painted and the other half in their original form; (b) Wave Surface (Wave-3); (c) Large rocks (LR1).

The concept of a rotational viscometer was utilized for the measurements presented here. The viscosity of the fluid used in the experimental setup is of no interest except that the chosen fluid had a viscosity that allowed for testing at typical temperatures and the expected range of τ. The PI-SWERL was operated over a test surface that was center-mounted onto a bearing and coupled to a fluid friction source (Fig. 1). As the test surface rotates in response to τ induced by the PI-SWERL, the viscosity of the fluid exerts a torque that eventually balances the action of τ. The amount of torque exerted by the fluid at varying rates of rotation of the test surface can be calculated accurately using Newtonian mechanics. In this manner, the magnitude of τ, measured in terms of torque that the PI-SWERL exerts onto surfaces of varying roughness can be measured at multiple rates of rotation of the PI-SWERL annular blade. The details of this measurement technique follow.

An aluminum disc (OD = 0.294 m) served as the mounting plate ("test plate") for test surfaces of varying roughness. Adhesives were used to glue various test surfaces to the test plate over the course of the experiments. The test plate could be coupled/decoupled from a hollow metal tube (OD = 0.0318 m, ID = 0.0284 m) by three countersunk screws. This tube was attached to a smaller tube (OD = 0.026 m) through a low-friction bearing, so that the annular gap between the tubes was 0.0012 m. The concentric tube assembly was immersed in a vegetable oil bath (container OD = 0.11 m). The annular region between the concentric tubes that was wetted with oil was 0.1 m. This component of the experimental setup is essentially equivalent in function to a rotational viscometer. When rotating, the largest portion of the frictional force on the test plate will originate from viscous drag between the two concentric tubes. Note that these dimensions were useful for designing a system with the range of desired characteristics, including size, rates of rotation, maintenance of laminar flow between concentric tubes, and other parameters. However, the exact values of dimensions, including the gap between the tubes, are provided for completeness of description of methods, but are not especially important since the entire setup undergoes an empirical calibration procedure to relate the magnitude of fluid friction to varying rates of rotation of the test plate. A thermocouple that was immersed in the oil provided a measure of the bath temperature at all times during testing. The entire test plate, concentric tube, and oil bath assembly was fastened to a table.

Using adjustable-height legs, a second flat surface ("PI-SWERL bench") with a circular cutout (D = 0.30 m) was placed on top of the table surface. The cutout in the PI-SWERL bench was fitted with guides so that when the PI-SWERL was placed on its bench, it would always be centered over the test plate. The adjustable height legs were varied to ensure that the annular blade was parallel with the test surface and that the test surface was just below the lowest part of the PI-SWERL, essentially emulating the distance between the annular blade and a real-world surface. The distance h between the annular blade and the test plate could be varied by sliding the annular blade up or down along the motor shaft. It was set at 0.0525 m for most of the tests to correspond to the lower limit of the likely distance between the annular blade and a test surface when the PI-SWERL is used in the field (estimated to be 0.054 m), but was also set at 0.0650 m for a subset of the tests to correspond to the upper limit of this distance (estimated to be 0.065 m). Results from measurements at these two heights for otherwise identical surfaces were used to ascertain that the effect of the distance h on the shear stress induced on the test surface is minimal. Note that for the laboratory tests, this distance was measured from the bottom of the annular blade to the aluminum test plate. Therefore, individual roughness elements were closer to the annular blade than the stated distance (by the value of their height). When used in the field, precise measurement of this distance is not possible at this time.

The relationship between the amount of DC power supplied and the RPM of the PI-SWERL annular blade was determined empirically and the power levels associated with desired target RPM levels were recorded. However, owing to day-to-day variations in motor response to the power supplied, it was not possible to exactly achieve target RPM values. Instead, the power needed to achieve a nominal target RPM was provided to the motor and the actual resultant RPM was measured accurately with an encoder on a one-second basis. Similarly, the rate of a rotation of the test plate was measured with an electronic pulse counter. The test plate sensor provided two pulses per rotation and was sampled once per second. Individual one-second measurements exhibited substantial noise owing to the coarse resolution of the pulse counter, especially at the low rates of rotation. However, this measurement noise was effectively reduced by averaging over multiple sampling intervals as described in Section 3.3.

3.1. Test protocol

Except where noted, the same test protocol was used for all measurements presented here. The viscosity of the oil used and hence the resultant fluid friction are temperature-sensitive. Therefore, all tests were started with a warm-up procedure, where the PI-SWERL annular blade was operated at maximum speed (≈8000 RPM) for a period of 15 min. The rotation of the test plate in response to the PI-SWERL operation provided a means to mix the oil thoroughly and bring its temperature to equilibrium with the ambient temperature. Whereas this initial step could result

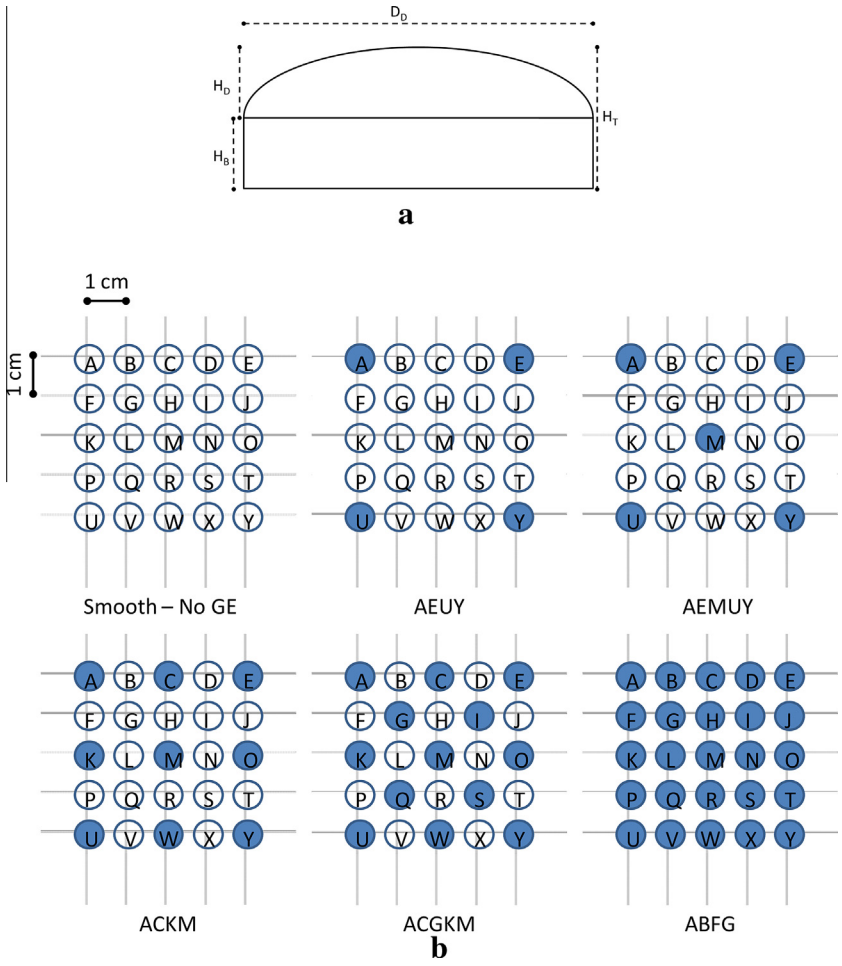

Fig. 4. (a) Dimensions of dome forms (GE); (b) illustration of varying roughness densities for GE and toothpick (TP) elements. Shaded circles illustrate where roughness elements would be glued.

in a temperature change (up or down) as large as 5 °C, the temperature for the duration of the test remained within ±0.3 °C of the equilibrium value achieved at the end of the warm-up period.

Prior to conducting a measurement with a new surface type the entire test plate assembly was weighed and the distribution of roughness over the test surface was noted. This information is required for calculating the moment of inertia, a critical parameter in subsequent data reduction (See Eq. (2) in Section 3.3 below). A typical example of an RPM test is shown in Fig. 2. Following the initial warm-up period, the power to the PI-SWERL is abruptly cut and the PI-SWERL is physically removed from its bench so that the influence of the decelerating annular blade is not felt by the test plate. The rotating plate is allowed to slow down and come to a stop on its own. This procedure is immediately repeated once again and is repeated twice at the end of the test. As explained later (See Eq. (4) and subsequent discussion in Section 3.3), these "decay" portions of the test are used to calibrate the apparatus. Between the first and last pair of "decay" tests, the power to the PI-SWERL is varied in a step-wise fashion to achieve seven nominal rates of annular blade rotation: 1000, 1500, 2500, 3000, 4000, 5000, and 6000 RPM. Each power setting is held for five minutes, which is adequate to ensure that the test plate response to the PI-SWERL annular blade rotation is at steady-state ($t_{characteristic} \approx 50$ s). The PI-SWERL is not removed from the test bench during this portion of the test procedure.

3.2. Test surfaces

Table 1 shows all of the different types of surfaces tested. There were five different types of roughness used. The first and simplest types of rough surfaces were sand paper of grit that varied from very rough (#12) to very smooth (#120); these were designated "SP-###", where "###" is the sand paper trade size. Sand paper was purchased in large sheets and cut to cover the entire test plate, except for a small circle in the middle of the plate (diameter 3 cm) where countersunk mounting screws are used to secure the test plate to the testing apparatus. The second type of roughness was achieved by gluing small dome-shaped forms to a test surface in varying surface densities (Fig 3a), defined as the percentage of the plan view area covered by the domes. Two sizes of domes were used (see Fig. 4a and Table 1): the larger (GE) was 7 mm in diameter and 2.9 mm in height and the smaller (GES) was 4 mm in diameter and 2.5 mm in height. The dome-like forms (eyes for toys) were used because they are nearly hemispherical, highly uniform, widely available in various sizes, amenable to being glued to surfaces, lightweight (filled mostly with air) – minimally impacting loading on bearings and test plate balance in measurement apparatus – and inexpensive. Five different patterns of roughness were created (Fig. 4b), which resulted in densities of domes that varied from sparse (AEUY) to nearly packed (ABFG).These types of roughness were labeled using the convention of the substrate (i.e., bottom surface) followed by the size of the domes (GE or GES)

Table 1
Roughness types tested.

Surface name	*n* tests h=5.25 cm/ *h* = 6.5 cm	Surface description	Roughness dimensions (mm) (average horizontal)	Roughness dimensions (mm) (Average vertical)	Rough-ness density (% area of test surface)	alpha	R^2	DF
Blank – smooth	2/2	Smooth Test Plate	N/A		N/A	1.010	0.987	15
SP-120	3/5	Sand Paper # 120 grit	0.13*	0.06*	>40%*	0.974	0.960	27
SP-80	2/1	Sand Paper # 80 grit	0.2*	0.12*	>40%*	0.986	0.963	15
SP-50	1/1	Sand Paper # 50 grit	0.35*	0.22*	>30%*	0.944	0.978	12
SP-36	2/2	Sand Paper # 36 grit	0.5*	0.3*	>30%*	0.915	0.992	21
SP-12	1/1	Sand Paper # 12 grit	2*	1.5*	>25%*	0.860	0.992	10
GE-AEUY	1/1	Smooth surface w/GE	D_D = 7	H_T = 2.9, H_D = 1.4, H_B = 1.5	2.4%	0.960	0.956	8
GE-AEMUY	1/1	Smooth surface w/GE	D_D = 7	H_T = 2.9, H_D = 1.4, H_B=1.5	4.8%	0.931	0.935	10
GE-ACKM	1/1	Smooth surface w/GE	D_D = 7	H_T = 2.9, H_D = 1.4, H_B = 1.5	9.6%	0.887	0.984	9
GE-ACGKM	1/0	Smooth surface w/GE	D_D = 7	H_T = 2.9, H_D = 1.4, H_B = 1.5	19.2%	0.859	0.988	4
GE-ABFG	2/2	Smooth surface w/GE	D_D = 7	H_T = 2.9, H_D= = 1.4, H_B = 1.5	38.5%	0.853	0.943	20
SP-120_GE-AEUY	1/0	120 Sand Paper w/GE	D_D = 7	H_T = 2.9, H_D = 1.4, H_B = 1.5	2.4%	0.949	0.961	5
SP-120_GE-AEMUY	2/0	120 Sand Paper w/GE	D_D = 7	H_T = 2.9, H_D = 1.4, H_B = 1.5	4.8%	0.922	0.989	10
SP-120_GE-ACKM	1/0	120 Sand Paper w/GE	D_D = 7	H_T = 2.9, H_D = 1.4, H_B = 1.5	9.6%	0.900	0.981	4
SP-120_GE-ACGKM	1/0	120 Sand Paper w/GE	D_D = 7	H_T = 2.9, H_D = 1.4, H_B = 1.5	19.2%	0.870	0.960	4
SP-120_GE-ABFG	1/0	120 Sand Paper w/GE	D_D = 7	H_T = 2.9, H_D = 1.4, H_B = 1.5	38.5%	0.866	0.961	4
SP-80_GE-AEUY	1/0	80 Sand Paper w/GE	D_D = 7	H_T = 2.9, H_D = 1.4, H_B = 1.5	2.4%	0.954	0.988	5
SP-80_GE-AEMUY	1/0	80 Sand Paper w/GE	D_D = 7	H_T = 2.9, H_D = 1.4, H_B = 1.5	4.8%	0.929	0.990	5
SP-80_GE-ACKM	1/0	80 Sand Paper w/GE	D_D = 7	H_T = 2.9, H_D = 1.4, H_B = 1.5	9.6%	0.902	0.982	5
SP-80_GE-ACGKM	1/0	80 Sand Paper w/GE	D_D = 7	H_T = 2.9, H_D = 1.4, H_B = 1.5	19.2%	0.878	0.972	5
SP-80_GE-ABFG	1/0	80 Sand Paper w/GE	D_D = 7	H_T = 2.9, H_D = 1.4, H_B = 1.5	38.5%	0.868	0.972	5
SP-50_GE-AEUY	1/0	50 Sand Paper w/GE	D_D = 7	H_T = 2.9, H_D = 1.4, H_B = 1.5	2.4%	0.933	0.997	4
SP-50_GE-ACKM	1/0	50 Sand Paper w/GE	D_D = 7	H_T = 2.9, H_D = 1.4, H_B = 1.5	9.6%	0.888	0.958	4
SP-50_GE-ACGKM	1/0	50 Sand Paper w/GE	D_D = 7	H_T = 2.9, H_D = 1.4, H_B = 1.5	19.2%	0.876	0.949	4
SP-50_GE-ABFG	1/0	50 Sand Paper w/GE	D_D = 7	H_T = 2.9, H_D = 1.4, H_B = 1.5	38.5%	0.866	0.970	5
SP-36_GE-AEUY	1/0	36 Sand Paper w/GE	D_D = 7	H_T = 2.9, H_D = 1.4, H_B = 1.5	2.4%	0.922	0.993	5
SP-36_GE-AEMUY	1/0	36 Sand Paper w/GE	D_D = 7	H_T = 2.9, H_D = 1.4, H_B = 1.5	4.8%	0.902	0.991	5
SP-36_GE-ACKM	1/0	36 Sand Paper w/GE	D_D = 7	H_T = 2.9, H_D = 1.4, H_B = 1.5	9.6%	0.885	0.946	4
SP-36_GE-ACGKM	1/0	36 Sand Paper w/GE	D_D = 7	H_T = 2.9, H_D = 1.4, H_B = 1.5	19.2%	0.868	0.969	5
SP-36_GE-ABFG	1/0	36 Sand Paper w/GE	D_D = 7	H_T = 2.9, H_D = 1.4, H_B = 1.5	38.5%	0.871	0.977	5
SP-36_GES-AEMUY	1/0	36 Sand Paper w/GES	D_D = 4	H_T = 2.9, H_D = 1.4, H_B = 1.5	1.6%	0.938	0.985	5
Wave-1	2/0	Wave Surface 1	Period = 25 mm	Amplitude = 4 mm	N/A	0.881	0.947	9
Wave-2	2/0	Wave Surface 2	Period = 50 mm	Amplitude = 7 mm	N/A	0.901	0.890	11
Wave-3	2/0	Wave Surface 3	Period = 75 mm	Amplitude = 7 mm	N/A	0.924	0.944	11
LR1	2/0	Large rocks	12 (estimate)	7 mm (Estimate)	25% (estimate)	0.848	0.944	6
LR1_shall	2/0	Large rocks – less exposed	12 (estimate)	5 mm (estimate)	25% (estimate)	0.860	0.950	6
SR1	2/0	Small rocks	5 mm (estimate)	2 mm (estimate)	25% (estimate)	0.889	0.986	5
TP-AEUY	1/0	Toothpick roughness	2	10	0.2%	0.918	0.978	5
TP-AEMUY	1/0	Toothpick roughness	2	10	0.4%	0.902	0.983	5
TP-ACKM	1/0	Toothpick roughness	2	10	0.8%	0.869	0.964	5
TP-ACGKM	1/0	Toothpick roughness	2	10	1.6%	0.842	0.915	5

* Estimated from Coated Abrasives Manufacturer's Institute (CAMI) standard specification Federation of European Producers of Abrasives (FEPA) and ISO 6344 approximate equivalents are P12, P36, P50, P80, and P120.

followed by the packing protocol (e.g., "AEUY" per Fig. 4). For example, "SP-80_GE-ACKM" refers to 7 mm domes (GE) that were glued to #80 grit sandpaper ("SP-80") in the pattern "ACKM" shown in Fig. 4, resulting in a surface density of 9.6% (see Table 1) whereas, "GE-ACKM" refers to the same dome configuration and density, but with the domes glued directly onto the smooth test plate. The third type of roughness consisted of toothpicks (TP, average diameter = 2 mm). Toothpicks were cut to 10 mm to emulate blades of grass and glued perpendicular to the test surface. The TP patterns that were examined included the same five patterns used with GE (see Fig. 4) as well as a pattern that emulates clumped blades of grass. The fourth set of roughness type examined was wave-like. Three wave-like surfaces (Fig 3b) with different amplitude and frequency were tested. These were intended to emulate the small ripples that are sometimes encountered when using the PI-SWERL on very sandy soils. Surfaces were constructed by gluing lengths of wooden dowels (diameter of 4 mm for wave-surface 1 or 7 mm for wave-surfaces 2 and 3) onto a stiff sheet of foam (cut to the size of the test plate) at specified inter-space distances (see Table 1). Dowels were cut at both ends so that they were flush with the edge of the foam. A flexible foam with thickness of ≈1 mm was used to create the wave-like surface by gluing the foam to the top of the dowels (serving as the guide for the wave crest) and to the stiff foam platform (serving as the trough guide).

The fifth type of surface (Fig 3c) was made using gravel of two different sizes. A surface was created in multiple steps. The test plate was traced on a piece of stiff, 5 mm-thick foam and the tracing was cut out and removed. This served as a form and was subsequently glued to another stiff foam piece (also 5 mm thick). The cutout of the test plate was partially filled with liquid glue and the appropriate amount of rock was dispersed into the glue by manual sprinkling. Once the glue set, the hardened glue, gravel, and base foam were cut out from the form and affixed onto the test plate. One such roughness element was created with small gravel (approximately 5–8 mm in size) and two (with varying levels of glue filler) were created with larger gravel (approximately 12–15 mm in size).

3.3. Data reduction

Each separate test included several decay observations (see Fig. 2b) that were used to calibrate the apparatus. The mass for each test surface configuration was used to calculate the moment of inertia of the entire rotating assembly with:

$$I = \frac{1}{2}M(r_1^2 + r_2^2) \tag{2}$$

where I is the moment of inertia [kg m^2], M is the mass [kg] of a thick-walled cylinder or annular disc, and r_1 and r_2 are, respectively, the inner (equals zero for solid disc) and outer radii of the cylinder or annular disc [m]. For a rotating object, the angular momentum is given by:

$$L = I\omega \tag{3}$$

where ω is the angular velocity [radians s^{-1}] and the torque T [N·m] is given by:

$$T = \frac{dL}{dt} = I\frac{d\omega}{dt} \tag{4}$$

Torque is the rotational analog to force just as moment of inertia and angular acceleration are the rotational analogs to mass and acceleration, respectively. Strictly, the angular velocity, angular momentum, and torque are vector quantities. However, for the apparatus described here, the only motion is rotation in one plane hence we have dropped the conventional vector notation. The decay curves shown in Fig. 2 visualize the response of the RPM as a function of time from the PI-SWERL operating at maximum speed followed by the abrupt removal of the PI-SWERL from the test bench. Once the PI-SWERL is removed, the torque acting on the test plate ($T_{\mathrm{cal},i}(\omega)$) as a function of test plate angular velocity can be calculated as the sum of the torques exerted by the fluid friction of the oil between the two concentric tubes ($T_{\mathrm{oil},i}(\omega)$), mechanical friction from the bearing and other sources ($T_{\mathrm{mechanical},i}(\omega)$), and air friction at the top ($T_{\mathrm{air\_top},i}(\omega)$) and bottom ($T_{\mathrm{air\_bottom,smooth}}(\omega)$) surfaces of the spinning test plate, so that:

$$T_{\mathrm{cal},i}(\omega) = T_{\mathrm{mechanical},i}(\omega) + T_{\mathrm{air\_top},i}(\omega) + T_{\mathrm{air\_bottom,smooth}}(\omega) + T_{\mathrm{oil},i}(\omega). \tag{5}$$

The subscript refers to a specific test i. Note that the torque due to the air friction on the bottom surface of the test plate does not change among the different tests. In principal, the torque due to friction from the mechanical bearing and the oil viscosity also should remain constant among the different surfaces tested. However, differences in the mass of the plate arising from various roughness surfaces influence the bearing friction and differences in steady-state operating temperature influence the oil's viscosity.

The relationship between ω and $d\omega/dt$ was obtained from the decay curves. In order to reduce the fluctuations in the one-second readings of ω, a 14-s moving average filter was applied to these data. The characteristic time of the decay curve is ≈50 s, so that the approximation of linearity over the 14-s smoothing interval that was used for ω (and $d\omega/dt$) is quite reasonable. Additionally, pairs of ω and $d\omega/dt$ values from all available decay curves for a set of tests were placed into one of 12 equal sized bins based on the value of ω. The bin interval size was selected so that the largest bin contains the largest value of ω as its midpoint. Within each bin, the average value of ω (and $d\omega/dt$) was calculated and used subsequently to obtain a relationship between the two variables. Bins that contained fewer than 10 data points were not used. The purpose of binning was to reduce the influence of the comparatively much larger number of observations associated with smaller values of ω. Fig. 5 shows an example of four decay curves completed as part of the same test and the results of a least squares fit for test i to the equation:

$$T_{\mathrm{cal},i}(\omega) = I_i\left.\frac{d\omega}{dt}\right|_i = I_i(b_i\omega + c_i) \tag{6}$$

where b and c are fitting coefficient. In all cases, values for the coefficient b were significant at the 0.05 level. In cases where the values for the coefficient c were not statistically significant at the

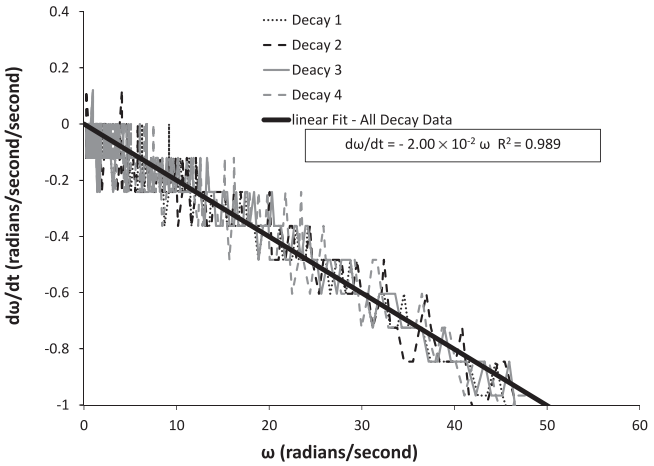

Fig. 5. Example decay curves and linear fit used in calibration for a single test sequence.

0.05 level, c was assumed to be zero and the regression was repeated without an intercept term. In cases where the value of c was significant at the 0.05 level, the relative advantage of including c in the regression versus using a linear fit without intercept was weighed using Akaike Information Criteria (Akaike, 1974). Out of 72 calibration regressions, in 25 cases non-zero values of c were retained. In all cases, P-values for the slope b were extremely small ($\ll$0.01) and in the 25 cases where an intercept was used, the highest P-value for c was 0.019, but in 22 of the 25 cases, P-values were less than 0.005.

Between the decay curves that were used to calibrate each test configuration i, the PI-SWERL net rate of rotation relative to the test plate/surface j (expressed as RPM) was held at a nominal value for a period of at least 5 min (Fig. 2) so that the test plate rate of rotation was at steady-state and all the torques acting on the system were in balance. This can be expressed by the equation:

$$T_{\text{PI-SWERL},i}[\omega_i(j)] = T_{\mathrm{mechanical},i}[\omega_i(j)] + T_{\mathrm{air\_bottom,smooth}}[\omega_i(j)] + T_{\mathrm{oil},i}[\omega_i(j)]. \tag{7}$$

Here the subscript "PI-SWERL" indicates that the torque is exerted by the operation of the PI-SWERL. Note that the right hand sides of Eqs. (5) and (7) differ only by one term. We assume here and demonstrate shortly that:

$$T_{\mathrm{air\_top},i}[\omega_i(j)] \ll T_{\mathrm{cal},i}[\omega_i(j)] \tag{8}$$

so that:

$$T_{\text{PI-SWERL},i}[\omega_i(j)] \approx T_{\mathrm{cal},i}[\omega_i(j)] = I_i\{b_i\omega_i(j) + c_i\}. \tag{9}$$

Eq. (9) serves as the basis for relating the torque exerted by the PI-SWERL on the test plate/surface to the rate of rotation of the test plate.

The validity of the assumption of Eq. (8) is examined with an illustrative example. Consider that the torque exerted by the PI-SWERL rotation at high RPM (e.g., 6000) is a factor of three or so larger for surface SP-12 than for the smooth plate surface (Fig. 6a). Therefore, if Eq. (8) was false, we would expect that if all the terms other than $T_{\mathrm{air/top},i}(\omega)$ in Eq. (5) were held constant, then $T_{\mathrm{cal,SP\text{-}12}}(\omega)$ would be considerably (e.g., 10% or more) larger than $T_{\mathrm{cal,Smooth}}(\omega)$. Instead, we find that when two tests that are close in time (i.e., with comparable mechanical friction from the bearing) and with nearly identical oil bath temperatures (i.e., with comparable oil fluid resistance) are compared at the highest rate of rotation of the smooth plate (corresponding to PI-SWERL RPM of ≈8000), the difference between $T_{\mathrm{cal,SP\text{-}12}}(\omega)$ and $T_{\mathrm{cal,Smooth}}(\omega)$ is

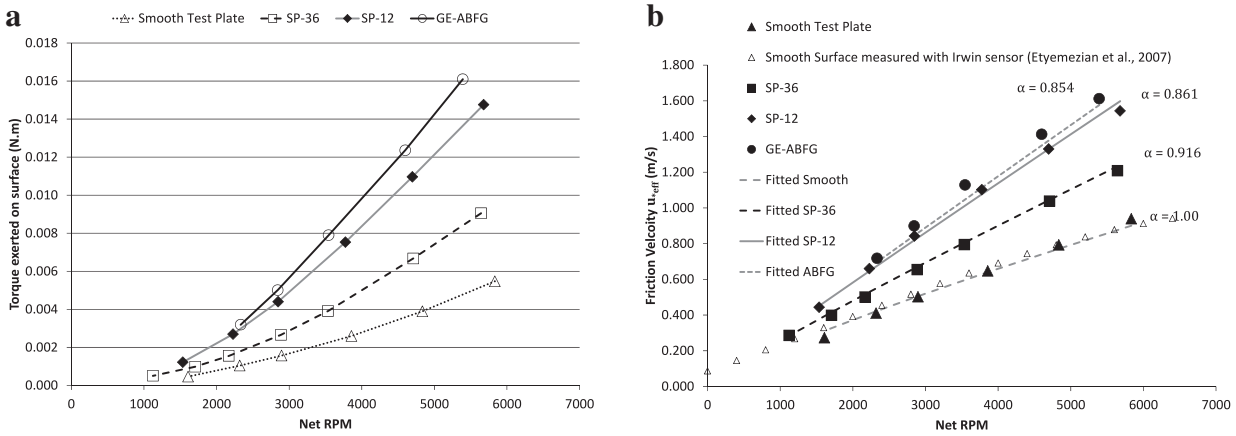

Fig. 6. Torque measured for surfaces of varying roughness and calculated $u_{*,\mathrm{eff}}$. (a) total torque on test plate/surface calculated with Eq. (9) and (b) Calculated $u_{*,\mathrm{eff}}$ within active region defined by vertical lines in Fig. 5b versus net RPM (PI-SWERL RPM minus RPM of test/plate/surface) for several different surface roughness types. Dashed lines correspond to fitted curves using Eq. (17).

≈1%; this is nearly negligible considering that it is smaller than the measurement precision of ≈5% based on replicate measurements with the same surface. Therefore, the assumption of Eq. (8) is considered valid in the present context. Note that this implies that the third term on the RHS of Eq. (5) is also essentially negligible.

4. Results and discussion

Fig. 6a shows the total torque exerted by the PI-SWERL onto the test surface. Note that since the shear stress induced by the rotation of the PI-SWERL blade acts predominantly in the tangential (θ) direction, the total torque and the average shear stress over the entire test surface are proportional. That is:

$$T_{\text{PI-SWERL},i}[\omega_i(j)] = C_0 \tau_{\text{i,average}}(\text{j}) \tag{10}$$

where we have introduced the symbol C_0 as a constant that does not depend on i or j.

Eq. (10) relates the total torque measured to the average shear stress over the entire test plate/surface. However, $\tau_{i,\text{average}}$ does not represent the value of τ that is "causing" the emissions as measured by the PI-SWERL. Moreover, the effective area over which wind erosion is simulated does not correspond to the total area of the test plate/surface.

One outcome of the present work is that an estimate of the effective area of dust emissions A_{eff} can be defined for future use. This is important because it allows for recasting absolute emissions measured with the PI-SWERL (units of mass of dust per unit time) as emission factors expressed on a per ground area basis (units of mass of dust per unit time per unit ground area). The effective area is arrived at by considering that the distribution of shear stress underneath the PI-SWERL annular blade and the nonlinear relationship between shear stress and dust emissions work together so that on the test surface, a contiguous area in the shape of an annular ring is overwhelmingly the main contributor to measured emissions at any given time.

In prior work, Etyemezian et al. (2007) described how the shear stress distribution under a larger version of the PI-SWERL (D = 0.57 m) was estimated using a series of profiling measurements with an Irwin-type sensor (Irwin, 1981). The Irwin sensor uses characteristics of the boundary layer to infer τ. Although not reported in Etyemezian et al. (2007), the same types of measurements were completed for the smaller version of the PI-SWERL described here. Fig. 7 shows the radial profile of the friction velocity u_* (see Eq. (1)), a quantity that is more widely used in aeolian sediment transport quantitation. Fig. 7b illustrates that there is an annular region that corresponds roughly to the PI-SWERL annular blade location and centered on a normalized radial distance (r/R) of 0.8 where the value of u_* is relatively constant. Fig. 7b also shows the modeled cumulative distribution of dust emissions as a function of radial distance for a PI-SWERL RPM of 2800 and various assumed values of threshold friction velocity u_{*t}. For the purposes of illustration, we have assumed that dust emissions per unit area per unit time E are roughly proportional to sand flux (e.g., Gillette et al., 2004) and that the sand flux can be described by the relationship given by Lettau and Lettau (1978) according to:

$$\begin{aligned} E &= J_0 \cdot (u_* - u_{*t}) \cdot u_*^2 \quad u_* > u_{*t} \\ E &= 0, \quad u_* \leqslant u_{*t} \end{aligned} \tag{11}$$

where J_0 is constant for a particular set of soil conditions. It is clear that most, but not all, of the emissions are expected to occur in the region underneath the annular blade. We state here and justify later that the region between the two vertical lines in Fig. 7b is considered as the active region for wind erosion measurement and that the effective area for calculating PI-SWERL emissions A_{eff} is given by:

$$A_{\text{eff}} = 0.875 \times \pi(0.15\ \text{m}^2 - 0.10\ \text{m}^2) = 0.035\ \text{m}^2 \tag{12}$$

Fig. 7c shows the error in the emissions estimate that would result from ascribing all of the measured emissions to a region with area equal to A_{eff} for different values of assumed u_*. In cases where the PI-SWERL RPM results in values of u_* that are everywhere less than u_{*t}, emissions are nonexistent and there is no error. Slightly higher values of RPM result in an underestimate of emissions by up to ≈12% and much higher values of RPM result in an overestimate of emissions by ≈12%. Put another way, without any knowledge of the threshold value for wind erosion, a ±12% error in the emissions estimate is introduced by assuming that only the portion of the test surface equal in area to A_{eff} is producing dust. Also shown in Fig. 7c as a function of PI-SWERL RPM is the Coefficient of Variation (defined as the standard deviation divided by the mean) of u_* between the two vertical bars in Fig. 7b.

The choice of active region that defines the effective area is not arbitrary. It is dictated by two competing effects. On the one hand, the region where u_* is highest and changes minimally with radial distance corresponds to the ideal region for accurately quantifying u_* that is causing the measured emissions. On the other hand, the narrower the gap between the two vertical lines shown in Fig. 7b, the greater is the uncertainty associated with the fraction of emissions that occur within that band. The present choice for effective area provides an acceptable uncertainty in the knowledge of the value of u_* that is causing the emissions and an acceptable uncertainty in the magnitude of the emissions per unit area per unit

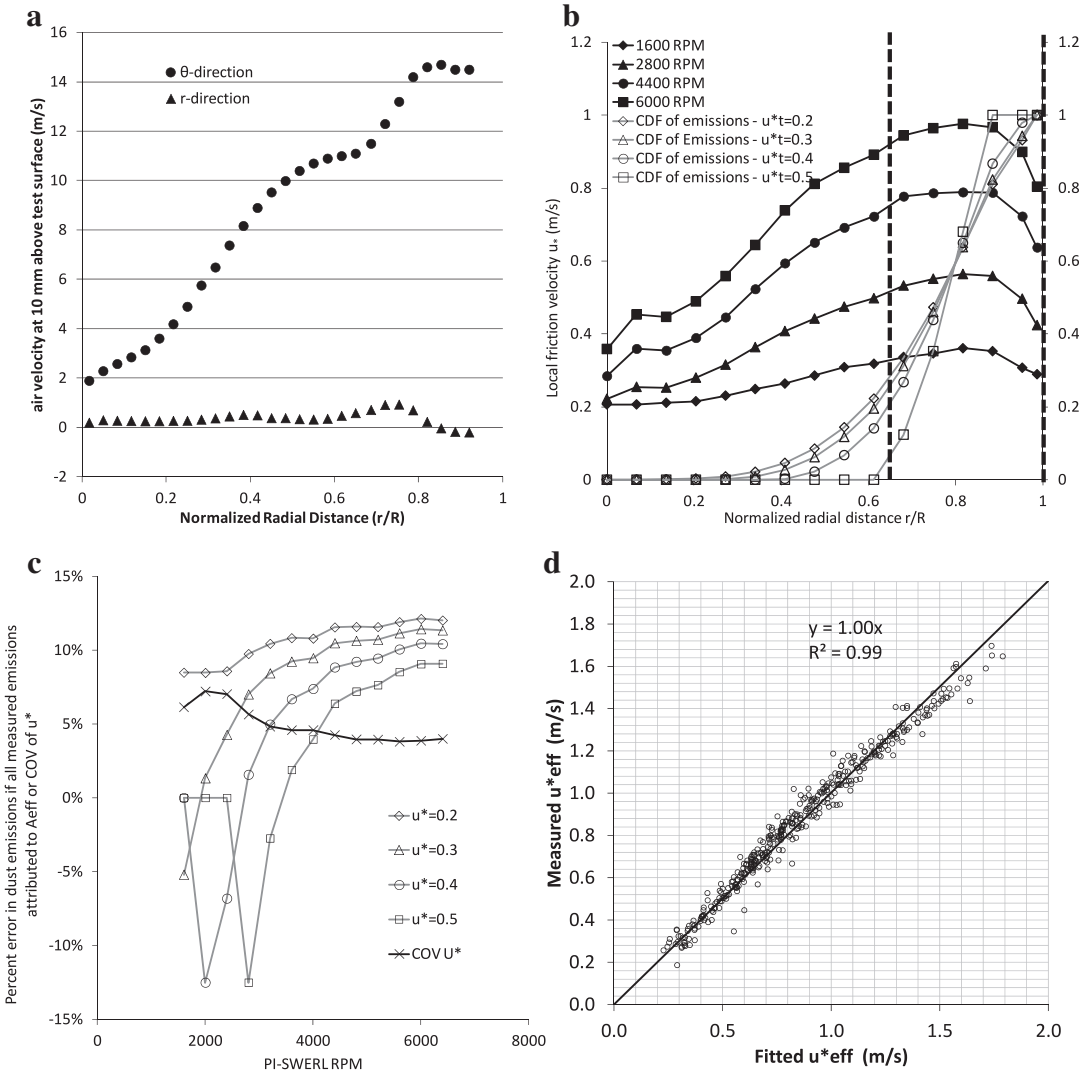

Fig. 7. Characteristics of τ and emissions in radial cross section. (a) wind velocity distribution measured with 2-axis hot wire anemometer probe at a height of 10 mm above the test surface and PI-SWERL RPM of 4000; (b) profiling measurements with Irwin-type sensor. Solid markers show the distribution of u_* at varying RPM. Open markers show the cumulative emissions up to a normalized radial distance r/R as a fraction of total emissions within the PI-SWERL for 2800 RPM and varying u_{*t}. The dashed vertical lines indicate the region considered to be active in simulating wind erosion ($0.67 \leqslant r/R < 1$); (c) Percent error in emissions resulting from assumption that emissions within PI-SWERL occur between radii corresponding to dashed vertical lines in (a). Also shown is the coefficient of variation (COV) of the friction velocity values that lie between the vertical lines; and (d) Measures $u_{*,\mathrm{eff}}$ versus value fitted with Eq. (18).

time. We state here without elaboration that the choice of effective area aims to minimize the uncertainty with which measured emissions and PI-SWERL RPM can be used to estimate the parameter J_0 in Eq. (11).

With the previous discussion in mind, the task of relating the direct measurement of torque with an induced τ begins with quantifying φ_T, the portion of the measured torque that is associated with the area of the test plate/surface that lies between the two vertical lines shown in Fig. 7a given by:

$$\varphi_T = \frac{T|_{r_1/R}^{r_2/R}}{T|_0^1} \tag{13}$$

This can be accomplished by integrating the torque from $0.67 \leqslant r/R < 1.0$ using the profiles of Fig. 7b and the relationship between the torque at a given radial distance, the shear stress at that distance, and the area A over which τ acts that is given by:

$$T(r) = \tau(r) \cdot dA \cdot r = \tau(r) \cdot r d\theta \cdot dr \cdot r \tag{14}$$

so that:

$$T|_{r_1}^{r_2} = 2\pi \int_{r_1}^{r_2} \tau(r) \cdot r^2 \cdot dr \tag{15}$$

For values of PI-SWERL RPM ranging from 1600 to 6400, the value of φ_T spanned a very narrow range from 0.795 to 0.807. Therefore, it was assumed that φ_T is independent of RPM and adequately represented by the value 0.80, the approximate midpoint of that range.

The average τ over the effective area A_{eff} was calculated from:

$$\varphi_T T_{\text{PI-SWERL},i}[\omega_i(j)] = C_0 \tau_{i,A_{\mathrm{eff}}}(j) \tag{16}$$

where the constant C_0 is given by:

$$C_0 = \frac{3}{2\pi(r_2^3 - r_1^3)}. \tag{17}$$

Fig. 6b shows the u_* values ($\sqrt{\tau_{A_{\mathrm{eff}}}/\rho}$) calculated for the same surfaces depicted in Fig. 6a. Through trial and error, it was found that a single parameter α could be used to describe the effect of roughness on u_* [m/s] versus PI-SWERL RPM curves through the equation:

$$u_{*,\mathrm{eff}}(\mathrm{RPM}) = C_1 \cdot \alpha^4 \cdot \mathrm{RPM}^{C_2/\alpha} \quad (18)$$

where C_1 is a constant equal to 0.000683 and C_2 is a constant equal to 0.832. Fitting values of α to the different surfaces tested resulted in root mean square error (RMSE) values for $u_{*,\mathrm{eff}}$ that ranged from 0.010 to 0.106 m s^{-1}, with a median RMSE of 0.028 m s^{-1} and a 95-percentile value of 0.085 m s^{-1}. The relationship between $u_{*,\mathrm{eff}}$ calculated from direct measurement and fitted through Eq. (18) for all tests and PI-SWERL RPM values tested is shown in Fig. 7d. The least squares linear regression (R^2 = 0.99, F(1, 395) = 115,000, P < 0.001) shown in the figure is for the equation that predicts the measured $u_{*,\mathrm{eff}}$ (y) from estimates of $u_{*,\mathrm{eff}}$ (x) obtained with Eq. (18). Values for the parameter α and the RMSE of the fit for each surface tested are given in Table 1.

It is noteworthy that there were no statistically significant differences found between tests conducted at the two different distances between the annular blade and the test surface (h = 0.0525 m and h = 0.0650 m). This was determined using the best fit for values of the parameter α as described above for test surfaces where there were measurements at the two heights (see Table 1). A paired, two tailed T-test (9 pairs of values from two different heights) was not significant at the 0.05 level (P = 0.054). These two heights are important since they were chosen to represent the range of distances between the PI-SWERL annular blade and the ground test surface that could result from the varying amount of compression that the PI-SWERL foam seal undergoes on different surfaces and as the seal ages and loses its elasticity. The finding of no statistically significant difference with the limited number of pairs available for comparison should not be interpreted to mean that there is no dependence at all of α on h. Rather, this difference if it exists is not resolved with the stated significance criteria. Note also that the results of this statistical test cannot be extended to values of h outside of the range stated.

5. Practical applications and limitations of roughness correction

A useful application of the information gathered in this study is a more accurate relation of PI-SWERL RPM to equivalent $u_{*,\mathrm{eff}}$ using information about the surface roughness. To date, investigators have had to rely on the calibration of PI-SWERL RPM over a smooth surface (Etyemezian et al., 2007). Recognizing that this led to a source of error for their data, Sweeney et al. (2008) applied a single correction factor – estimated roughly by invoking similarities between the PI-SWERL flow regime and Couette flow – for the surfaces that were among the roughest they tested. A more systematic approach for applying a rough surface correction has not been available to date.

It can be seen from Fig. 6b that the error in using the smooth surface calibration regardless of surface roughness can lead to substantial underestimates of $u_{*,\mathrm{eff}}$. Underestimating the u_* at which a measurement is being conducted has the effect of ascribing much higher dust emissions to a rough surface than would actually be occurring at that (underestimated) value of u_*.

The most direct method for correcting for roughness would be to use a reproduction of the surface of interest in the same types of laboratory tests that were conducted in this study. Recently, it has become possible to use LiDAR technology to obtain highly detailed, three-dimensional representations of real surfaces with resolutions on the order of one millimeter or less (Aguilar et al., 2009). Therefore in principal, a surface of interest can be scanned by lidar in the field and the surface reconstructed using a three-dimensional printer – also increasingly available. The reproduced surface can then be tested directly in a viscometer-type device similar to the one used to complete measurements in this study.

Here, we propose two methods for applying a correction to the smooth surface calibration that accounts for the roughness of the tested surface. The first method relies on using the surfaces described in Table 1 as templates for assessing where in the roughness regime a particular soil surface might be best described. The second method uses a more quantitative photogrammetric approach.

5.1. Method 1: surface lookup table

The surfaces described in Table 1 span a considerable range of small-scale roughness types that can be encountered in the field. For the most part, they are also well-defined and easy for researchers to recreate with minimal materials for the purpose of a tactile reference point in the field. Note that due to the size of the PI-SWERL, it would not be possible to operate the instrument on roughness elements with a physical height larger than a few centimeters, so that the range of surfaces that are encountered in the field and can be tested with the PI-SWERL is reasonably represented by the entries in Table 1.

Since no real surface will be identical to the contrived roughness arrangements that were part of the current tests, it is probably more useful to classify the surfaces into sub-categories of roughness, ranging from nominally smooth to maximally rough. In this way, a number of different surfaces can be referenced to determine which category the surface of interest is best placed in. The choice for categorization is somewhat arbitrary; here we propose five categories (A–E, smoothest to roughest) based on the value of α (see Table 2). For example, the salt-crusted playa surface shown in Fig. 8a resembles SP-12 and SR1, both of which are in Category D. The surface shown in Fig. 8b more closely resembles LR1 and probably should be placed in category D. Fig. 8c depicts a rippled dune surface and can naturally be compared to Wave 2 or Wave 3 surfaces (borderline between Categories B and C). Categorization of Fig. 8d is less straightforward since none of the surfaces tested here resembles a cracked silt/clay crusted playa. However, here too, a researcher with reasonable experience with boundary layer properties would presume the surface is somewhat smooth (Category A or B).

Clearly, this subjective method of estimation of roughness is not ideally accurate and it is quite possible that an error can be made in category placement. This error ε can be quantified in a relative way with the equation:

$$\begin{aligned}\varepsilon &= \Delta\alpha \cdot \frac{du_{*,\mathrm{eff}}/d\alpha}{u_{*,\mathrm{eff}}} \\ &= \Delta\alpha \frac{C_1 \cdot 4 \cdot \alpha^3 \cdot \mathrm{RPM}^{C_2/\alpha} + C_1 \cdot \alpha^4 \cdot \ln(\mathrm{RPM}) \cdot \mathrm{RPM}^{C_2/\alpha} \cdot (-C_2/\alpha^2)}{C_1 \cdot \alpha^4 \cdot \mathrm{RPM}^{C_2/\alpha}} \\ &= \Delta\alpha \cdot \frac{4 - \ln(\mathrm{RPM}) \cdot (C_2/\alpha)}{\alpha}\end{aligned} \quad (19)$$

The effect of RPM and value of α on ε is shown in Fig. 9 for an error equivalent to the span of a category (i.e., $\Delta\alpha$ = 0.04). The error increases with increasing values of RPM and with decreasing values of α. If we limit ourselves to reasonable values of u_* (<1.2 m s^{-1}), then for a rough surface (α = 0.82) at 3150 RPM, an error of ±21% results in an estimate of $u_{*,\mathrm{eff}}$ from incorrectly categorizing the surface roughness by one full category in Table 2. This is probably an upper end estimate of the error because for smoother surfaces, the error is smaller and because a researcher with some experience in assessing surfaces for roughness can probably categorize a particular surface more adeptly than within ±1 full category of the correct estimate. However, this latter assertion has not been tested as part of this study. It is also worth noting that generally surfaces that have substantial non-erodible, roughness

Table 2
Suggested grouping of roughness types by value of α.

Range of values of α	Roughness category	Description of approximate range of roughness covered.
$\alpha \geqslant 0.96$	A: Use 0.98	Smoother end: polished aluminum plate, 120 grit sandpaper* Rougher end: 60 grit sandpaper* (not tested); sparsely populated with dome-shaped roughness (7 mm, GE-AEUY)** Example: silt–clay crusted dry lake bed with minimal cracking and sparse gravel (< 2.5% cover)
$0.96 > \alpha \geqslant 0.92$	B: Use 0.94	Smoother end: 60 grit sandpaper* (not tested), sparsely populated with dome-shaped roughness (7 mm, GE-AEUY)** Rougher end: 36 grit sandpaper; populated with dome-shaped roughness (7 mm, GE-AEUY)** Example: Typical sandy loam desert soil with less than 5% gravel cover.
$0.92 > \alpha \geqslant 0.88$	C: Use 0.90	Smoother end: 36 grit sandpaper; populated with dome-shaped roughness (7 mm, GE-AEUY)** Rougher end: 20 grit sandpaper* (not tested); populated with dome-shaped roughness (7 mm, GE-ACKM)** Example: Soil with less than 10% gravel cover; loose sand with small ripples (7 mm crest to trough)
$0.88 > \alpha \geqslant 0.84$	D: Use 0.86	Smoother end: 20 grit sandpaper* (not tested); populated with dome-shaped roughness (7 mm, GE-ACKM)** Rougher end: 12 grit sandpaper*; dense, dome-shaped roughness (GE-ABFG)** Example: gravel cover (10% - 35%).

* Estimated from Coated Abrasives Manufacturer's Institute (CAMI) standard specification. Federation of European Producers of Abrasives (FEPA) and ISO 6344 approximate equivalents are P12, P36, P50, P80, and P120.
** Refer to Table 1 for surface description.

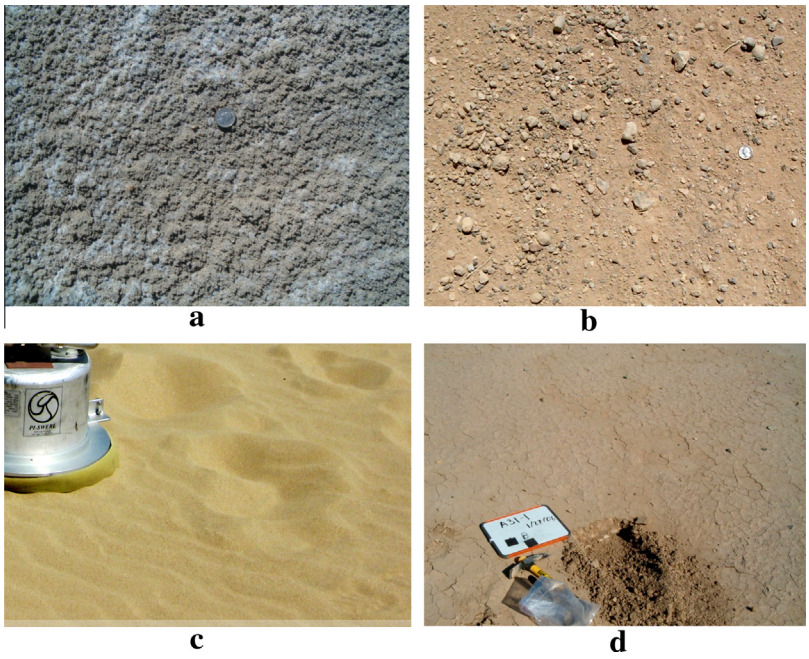

Fig. 8. Example surfaces encountered during field measurements. (a) Salt crusted playa (photo credit: Mark Sweeney); (b) Gravel covered loose soil (photo credit: Mark Sweeney); (c) Rippled dune surface (Photo credit: Vicken Etyemezian); and (d) Silt-crusted playa with cracks (Photo credit: Vicken Etyemezian).

elements (Category E) larger in size than a few millimeters are usually not prone to wind erosion (Gillette, 1999).

5.2. Method 2: photogrammetric estimation of roughness correction

For applications that require more stringent levels of accuracy for estimating $u_{*,\mathrm{eff}}$, we examined the incremental improvement in accuracy offered by a simple photogrammetric method for quantifying the effect of roughness on α. The method uses computer software (MATLAB™) to estimate the parameter α from a series of photographs. There is substantial detail in the image processing that is required for this technique. Since the aim is only to provide an overview of how the technique is implemented and since the method is still under development, we omit the low-level details of implementation and provide only a high-level description of the procedure.

For each surface examined, several color photographs were obtained using an inexpensive digital camera (Canon, PowerShot A490). An opaque box was placed on the surface of interest. The camera lens was inserted into a hole at the top of the box so that the distance between the camera and the surface was 0.40 m. A 0.7 m long, 0.2 m diameter tube was inserted into a hole at the side of the box and elevated with respect to the ground at an angle θ ("illumination angle" hereafter). A lamp with a 13-W compact fluorescent bulb was attached to the open end of the tube to illuminate part of the surface. This tube arrangement serves as an approximation to a collimating lens that casts light with a narrow spread onto the surface of interest at an angle of 56.9° (θ) with respect to the horizontal.

A black and white marker with attributes that are convenient for automatic identification by the image processing software was laid on top of the test surface and used subsequently to scale the photograph. Five photographs were obtained for each surface tested. After each photograph, the test surface was manually rotated ≈22.5° so that by the end of the fifth photograph, the test surface had been rotated 90°. Images of the test surfaces were subsequently transferred to a desktop computer for further processing.

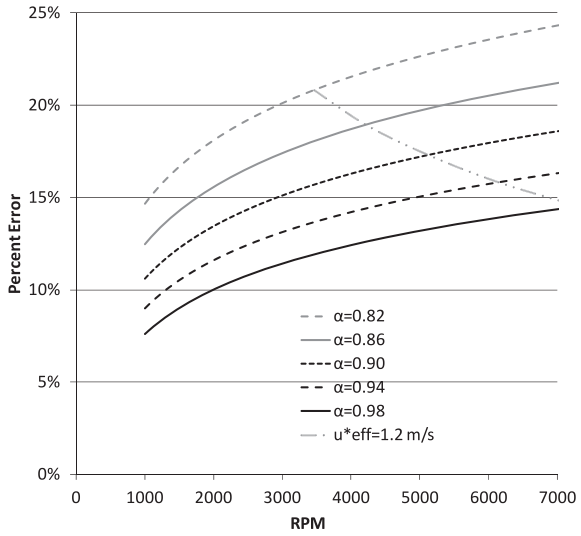

Fig. 9. Percent error is $u_{*,\mathrm{eff}}$ associated with an error in α equivalent to the span of a category in Table 2 ($\Delta\alpha = 0.04$). Also shown is the RPM at which $u_{*\mathrm{eff}}$ is equal to 1.2 m/s.

The choice of the specific value of the illumination angle (θ) was not altogether arbitrary and it is noteworthy that the results of the analysis likely depend on this choice. Ideally, multiple illumination angles would have been used so that the three dimensional nature of the roughness would be captured more fully. Chappell et al. (2010) examined the effect of the illumination angle as well as the azimuth angle (horizontal projection of the direction of illumination) on the shadow cast onto a horizontal plane by rough surfaces. Naturally, they found that the fraction of the surface that was still illuminated (which they define through a shadow function) when viewed at nadir decreases with increasing illumination angle and this dependence was not independent of the type of roughness examined. The work of those authors, substantially more in-depth than the comparatively cursory technique used here, relied on reconstruction of surfaces using mathematical software and calculation of shadows with the aid of this software, essentially with limitless numerical resolution. The present study used an inexpensive digital camera with finite resolution (12 Megapixels). Thus, a compromise had to be struck between two competing interests. The size of the smallest shadow of interest had to be resolvable with the camera used. This was balanced with the need to use the smallest illumination angle achievable, because the smaller the illumination angle, the less objects will be likely to shadow one another; that is, at higher illumination angles, information is lost because larger objects may shadow smaller ones. Ultimately an illumination angle of $\approx 60°$ ($\theta = 56.9°$) was chosen. Accounting for the subsequent filtering to eliminate identification of spurious shadows, this choice enabled the resolution of shadows as small as 0.07 mm in length, or objects that are $\approx$0.1 mm in height. Objects <0.1 mm in height were deemed likely too small to protrude above the viscous sub-layer and therefore unlikely to contribute to the drag to any appreciable extent.

The processing of photographs was based on the analysis of shadows cast by roughness elements when they are illuminated at an oblique angle. Once started, the image processing is mostly automated through a custom program, with a limited need for user intervention. An example photograph is shown in Fig. 10 along with the intermediate images used in the processing algorithm. Fig. 10a is the photograph as obtained by the digital camera. In Fig. 10b, the scaling marker has been identified and an area that is illuminated (but does not include the scaling marker) has been isolated for the analysis. The scaling marker is used to determine how many square millimeters are represented by each pixel in the photo. For the example shown, each pixel is equivalent to 1.4×10^{-3} mm^2. In Fig. 10c, the color photograph has been converted to a grayscale image and a contrast threshold has been specified to identify pixels that correspond to shadowed regions.

In the next set of steps, contiguous white regions (corresponding to shadows) are flagged if they are above a size threshold, the area covered by the "aerodynamic influence zone" (AIZ) – related to but different from the actual optical shadow as explained below – for each region is calculated, pixels within the AIZ of each flagged region are removed from further consideration, and the process is repeated for successively smaller size thresholds. For the preliminary work shown here, seven size thresholds were used corresponding to elements that are >10 mm in nominal height, 7–10 mm, 4–7 mm, 2–4 mm, 1–2 mm, 0.4–1 mm, and 0.1–0.4 mm. The nominal height corresponding to each contiguous region of pixels representing a shadow was estimated by: 1. calculating the center, major axis length, minor axis length, and inclination angle (angle formed between major axis and horizontal) of an ellipsoid with an equivalent area and the second moment as the region of pixels being considered, 2. calculating the projection of the major and minor axes onto the horizontal, 3. obtaining the root mean square of the two projections, and 4. using the illumination angle to calculate the height of the roughness elements. There may be numerous other methods to estimate the height of individual roughness elements, but the method described was adequate for the preliminary nature of this aspect of the study.

Fig. 10d and e are essentially identical to Fig. 10c, because in the example shown, no roughness elements with nominal height >7 mm were identified. However, four elements with nominal height between 4 and 7 mm were identified (Fig 10f). The projected areas associated with each of the ellipsoids representing each of those four roughness elements were calculated. Moreover, a region corresponding to the AIZ was removed (blackened) from further consideration. This was accomplished by assuming that the AIZ width was equal to the width of the optical shadow of the roughness element and AIZ length was some multiple, s, of the nominal height of the roughness element (s = 8 in Fig. 10 for illustrative purposes only, but s = 2 for actual calculations as explained below). This concept of AIZ stems from observing that the region in the lee of a bluff body is characterized by a wake bubble (e.g., Hanna et al., 1982, pp. 20–21) where the turbulent boundary layer is detached from the surface. We have assumed here that smaller roughness elements that are located within the AIZ of a large roughness element will have a minimal impact as momentum sinks since they are not in contact with the separated boundary layer. Accordingly, the light shadows of smaller elements found within the AIZ of larger elements should be omitted from consideration. The specific value of s used for illustration purposes in Fig. 10 (s = 8) is somewhat larger than what the wake bubble size (Hanna et al., 1982, pp. 20–21) might suggest would be an appropriate size for a reduced τ zone ($s \approx 2.5$) for a hemispherical shape and smaller than 10 (approximately the limit in the case of a strictly 2-dimenional object like a fence). In any case, it was found that the relationship between α and AIZ (e.g., Fig. 11) did change for values of s between 1 and 2, but was invariant (except for the magnitude of a proportionality constant) for the range of values of s 2–10. It is expected that a different set of surface roughness types might have provided a more clear-cut choice for the value of s. Note that an AIZ that is interrupted by the left edge of the region being analyzed "wraps" around to the right edge (see right side of Fig. 10f). The remaining panels in Fig. 10 correspond to the identification and AIZ-casting of elements in successively smaller height bins.

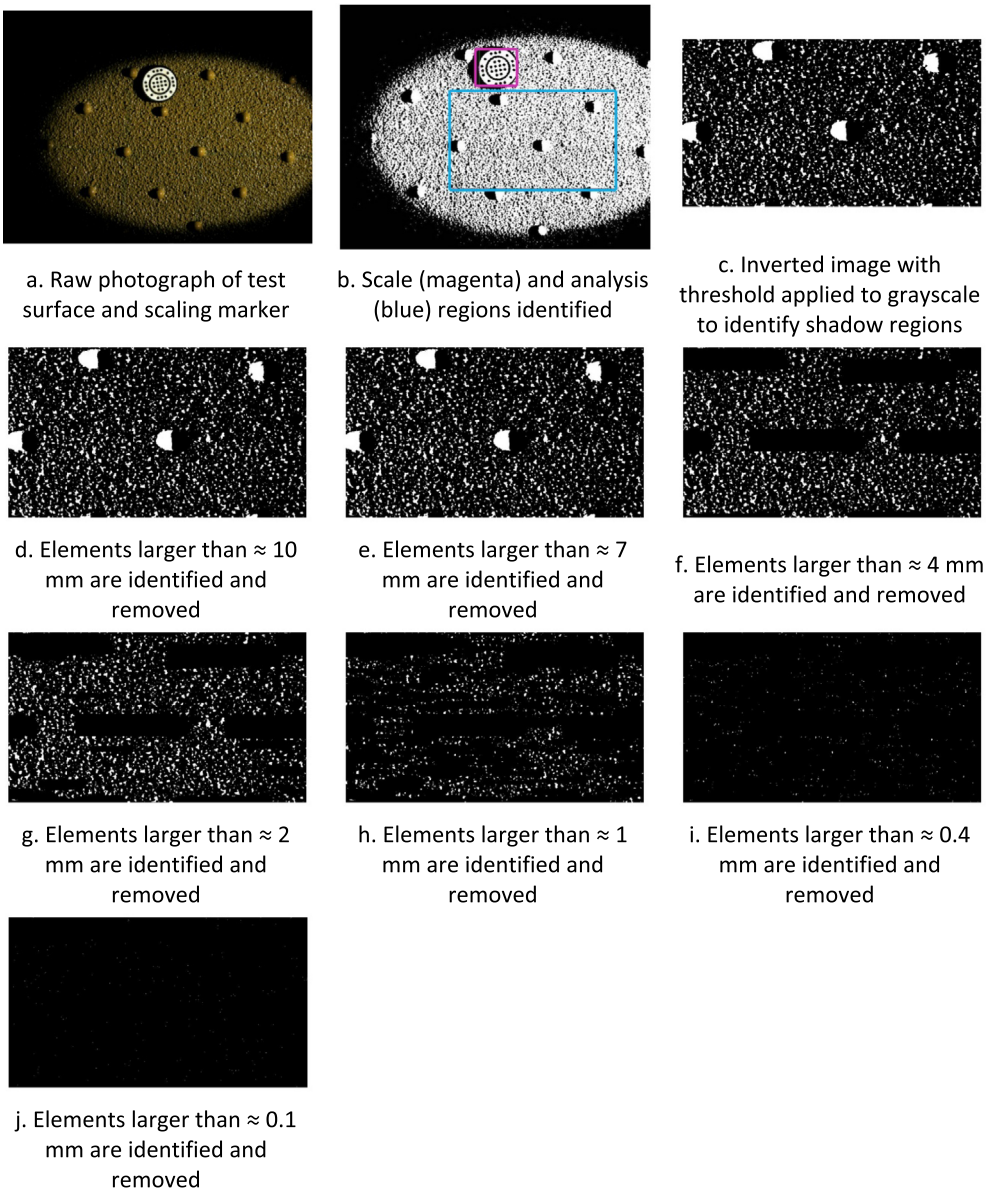

Fig. 10. a. Photograph of surface with dome forms mounted on 36 grit sandpaper (SP-36_GE-ACKM), and b–j. images resulting from successive steps in image processing algorithm.

Owing to the large number of variables and the relatively small number of different surface roughness types examined during this study, several simplifying assumptions were made in relating the results from photogrammetric analysis to the corresponding effect on the u_*-RPM PI-SWERL relationship. First, the size of the AIZ was assumed to be twice the size of the roughness element (i.e., $s = 2$). Physically, this translates into assuming that the wake bubble behind a roughness element is equal in size to the element and that smaller roughness elements within that wake bubble should not be considered as contributors to the shear stress experienced by the surface as a whole. It is noteworthy that the choice of AIZ multiplier is somewhat arbitrary, but in line with previous work on bluff bodies in turbulent boundary layer flow (Hanna et al., 1982). Second, even though the roughness elements were analyzed in terms of seven size bins, the relatively small dataset required aggregation of the results into two size bins. Roughness elements were considered either "large" or "small" with the subscripts "l" and "s" referring to entities related to those roughness sizes, respectively. Thus, A_l was calculated as the sum of AIZ areas as a percentage of total plan area for all roughness elements in the >10 mm, 7–10 mm, 4–7 mm, 2–4 mm, and 1–2 mm nominal height size bins. Similarly, A_s was calculated as the sum of the percentage of the total plan area occupied by the AIZ of all roughness elements in the 0.4–1 mm and 0.1–0.4 mm nominal height bins.

Fig. 11 shows the value of the parameter α from Eq. (17) plotted against A_l. Note that for these calculations A_l was obtained by averaging the results of photogrammetric analysis for all of the photographs taken for each surface (i.e., the five photographs taken after successive rotations of 22.5°) First, only those surfaces where the fraction of plan area covered by small roughness elements (A_s) was less than 0.05 were considered in order to isolate the effects of the large roughness elements. Noting that the upper limit of A_l is unity and further noting that the effect of increasing A_l past a value of ≈0.4 does not appear to have an effect on α, an additional assumption is made that the relationship between A_l and α_l (i.e., α for large A_l) can be approximated by:

$$\alpha_l = 0.85 + (1 - 0.85) \cdot e^{-6.9A_l} \quad (20)$$

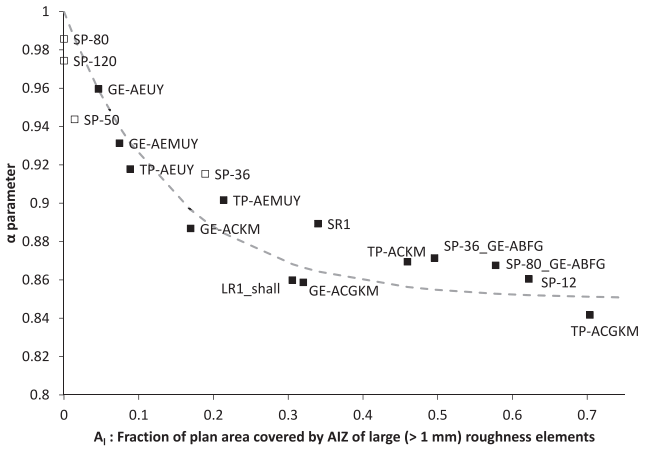

Fig. 11. Fitting parameter α from Eq. (17) versus the fraction of plan area (Al) covered by the aerodynamic Influence Zone (AIZ) of roughness elements with nominal height > 1 mm. The AIZ is determined as a multiple ($s = 8$) of roughness height. Physical roughness heights were estimated from photographed shadows of surfaces that were illuminated at an angle θ of 56.9°. Dashed line represents Eq. (19) fit. Surfaces with less than 0.05 of the fraction of plan area covered by elements <1 mm are shown as solid squares to isolate effects of the two sizes (A_l and A_s) considered.

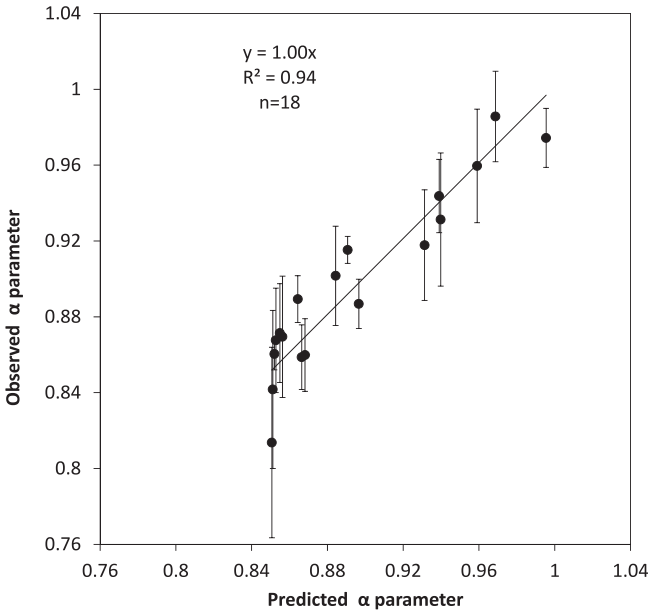

Fig. 12. Observed α parameter (from best fit to Eq. (17)) and predicted α parameter using photogrammetric methods and Eq. (21). Vertical bars are the standard error of the fit to α using Eq. (17).

which presumes a limiting value for α_l of 0.85 for large A_l. This assumption is known not to hold at the highest values of A_l since an increase in roughness density beyond some intermediate value begins to result in a decrease in effective aerodynamic roughness (e.g., Marshall, 1971; Shao and Yang, 2008).

There were only three surfaces tested where the AIZ from the smaller roughness elements (<1 mm) occupied a larger fraction of the plan area than those from larger elements ($\geqslant$1 mm). Therefore, rather than using a best fit to obtain the equivalent of Eq. (19) for small roughness elements, we observe instead that the SP-50 surface had a value for A_S of 0.43 and a corresponding value of α_s (i.e., α for small A_s) of 0.939. In the absence of additional information a simple linear relationship is proposed:

$$\alpha_s = \text{maximum}\left(0.939, 1 - \frac{1-0.939}{0.43} \times A_s\right) \quad (21)$$

where we have assumed that α_s cannot be <0.939 for small roughness elements.

Finally, it is proposed that the combined effect of α_l and α_s for cases where there are roughness elements in both sizes, denoted by α_{eff} be calculated by:

$$\alpha_{eff} = \text{minimum}(\alpha_l, \alpha_s) \quad (22)$$

Values of α_{eff} calculated with Eq. (22) are compared to the values observed (estimated from Eq. (17)) in Fig. 12. The vertical bars in the figure represent the standard error of the value of α_{eff} obtained by fitting to Eq. (17). The absolute mean error (AME) associated with predicting α_{eff} with Eq. (22) is 0.017 for all of the surfaces examined, which is better than the 0.04 value that was assumed for the surface lookup table method above.

All of the analyses pertaining to shadows discussed here have been based on the average shadow parameters over five azimuth angles that span ¼ of a circle (0°, 22.5°, 45°, 67.5°, and 90°), but a single zenith illumination angle (56.9°). In the case of the azimuth angle, it was assumed that a rotation over 90° would be sufficient to capture any anisotropy of the surface. This was true for the surfaces examined here, but not necessarily true for many natural surfaces. In general, the relationship between aerodynamic parameters (e.g., AIZ) and shadow parameters is going to vary with the range of azimuth illumination angles considered as well as the zenith illumination angle. For modeling aerodynamic roughness height (z_0) of a natural surface using shadow analysis, Chappell et al. (2010) opted to integrate the shadow parameters over all illumination angles in both the zenith and azimuth dimensions. The approach of Chappell et al. (2010) ought to be adopted in the further development of the photographic technique described here.

The method presented above for simple photogrammetric estimation of surface roughness effects on the PI-SWERL u_*/RPM relationship is not intended to be prescriptive. In addition to several assumptions, the number of different types of surfaces examined does not span a wide enough range of roughness elements in terms of geometry, density, and combination of sizes. However, it does indicate that the development of similar methods as part of a more extensive study may be warranted. Whereas we have limited our attention here on the relationship between photogrammetric parameters that inform on surface roughness and τ that the PI-SWERL imparts at varying RPM, the photogrammetric technique can be expanded to include assessment of aerodynamic roughness at the field scale. Chappell et al. (2010) were able to show that photogrammetric parameters could be related to the aerodynamic roughness to physical roughness height ratio using the wind tunnel data of Dong et al. (2002). It would be worthwhile to expand the digital photography technique described here and apply it to estimate aerodynamic roughness on the field scale at locations where z_0 is measured independently in a manner similar to what Chappell et al. (2010) suggest.

6. Conclusions

This study has addressed a number of outstanding questions regarding the interpretation of PI-SWERL measurements. It was demonstrated that potential errors in emissions of dust were approximately 12% when ascribing all of the emissions measured by the PI-SWERL to an effective area equal to 0.035 m^2 (where τ was relatively constant over an annulus with an inner radius of 0.20 m and an outer radius of 0.30 m).

The relationship between PI-SWERL rate of rotation (expressed as RPM) and $u_{*,eff}$ was, as expected, found to be dependent on the

roughness of the surface. A series of measurements using a device similar to a viscometer indicated that the effect of surface roughness on this relationship could be embodied in a single parameter α, which ranged between a high value of unity for smooth surfaces and a low value of 0.85 for the roughest surfaces tested. The same measurement technique was used to investigate the effect of small variations in the distance between the PI-SWERL annular blade and the test surface. Such variations may be encountered in field settings as a result of the observed change in compressibility of the elastomeric foam used to seal the PI-SWERL to the test surface or due to unevenness in the test surface. It was found that there were no statistically significant differences for changes on the order of 0.01 m in the distance between the blade and the surface.

Two techniques for accounting for surface roughness in estimating the equivalent $u_{*,\mathrm{eff}}$ exerted at a particular PI-SWERL RPM were investigated. In the first method, it was assumed that an experienced field scientist would be able to compare a test surface of interest to a gallery of surfaces that were tested and summarized in the present work. It was assumed without formal justification that the error in estimating the parameter α would be less than 0.04, which is roughly equivalent to 20% at 3000 RPM. The second method used a simple photogrammetric technique to relate physical roughness parameters to the parameter α. Although a number of simplifying assumptions were invoked and only a limited combination of surface roughness geometries were examined, the method did appear to reduce the uncertainty in estimating α by $\approx$50% as compared to the first method. In the authors' view, the preliminary success in implementing this photogrammetric method warrants further, more targeted investigations and efforts to develop this technique for the small roughness elements considered in this study.

The focus of the present study has been on methods to correct for roughness when determining the relationship between PI-SWERL RPM and equivalent u_*. However, it is possible that the direct measurements of shear stress and the methods used to estimate shear stress can also be utilized in the broader contexts of estimating aerodynamic roughness length and surface drag coefficients. The former is useful for estimating u_* from wind speed at a given height. The latter may be useful for estimating important parameters used in shear-stress partitioning models, such as the one proposed by Raupach et al. (1993).

Acknowledgements

This research was supported by the Arid Lands Research Center, Tottori University, Tottori, Japan through the Global Center of Excellence (GCOE) for Dryland Science program; the Strategic Environmental Research Program (SERDP) through project RC-1729; and the Particulate Emissions Measurement Laboratory (PEML), Desert Research Institute.

References

Aguilar, M.A., Aguilar, F.J., Negreiros, J., 2009. Off-the shelf laser scanning and close-range photogrammetry for measuring agricultural soils microrelief. Biosyst. Eng. 103 (4), 504–517.

Akaike, H., 1974. A new look at the statistical model identification. EEE Trans. Autom. Contr. AC-19, 716–723.

Bagnold, R.A., 1941. The Physics of Blown Sand and Desert Dunes. Chapman and Hall, London.

Brown, S., Nickling, W.G., Gillies, J.A., 2008. A wind tunnel examination of shear stress partitioning for an assortment of surface roughness distributions. J. Geophys. Res. Earth 113, F02S06.

Chappell, A., Van Pelt, S., Zobeck, T., Zhibao, D., 2010. Estimating aerodynamic resistance of rough surfaces using angular reflectance. Remote Sens. Environ. 114, 1462–1470. http://dx.doi.org/10.1016/j.rse.2010.01.025.

Chepil, W.S., 1950. Properties of soil which influence wind erosion: I. The governing principle of surface roughness. Soil Sci. 69, 149–162.

Dong, Z., Liu, X., Wang, X.M., 2002. Aerodynamic roughness of gravel surfaces. Geomorphology 43, 17–31.

Eitel, J.U.H., Vierling, L.A., Long, D.S., 2010. Simulatneous measurements of plant structure and chlorophyll content in broadleaf saplings with a terrestrial laser scanner. Remote Sens. Environ. 114, 2229–2237.

Etyemezian, V., Nikolich, G., Ahonen, S., Pitchford, M., Sweeney, M., Gillies, J., Kuhns, H., 2007. The Portable In-Situ Wind Erosion Laboratory (PI-SWERL): a new method to measure PM_{10} windblown dust properties and potential for emissions. Atmos. Environ. 41, 3789–3796.

Colebrook, C.F., 1939. Turbulent flow in pipes, with particular attention to the transition between the smooth and rough pipe laws. J. ICE 11 (4), 133–156.

Flack, K.A., Schultz, M.P., 2010. Review of hydraulic roughness scales in the fully rough regime. J. Fluids Eng. 132, 041203–041210.

Gillette, D., Ono, D., Richmond, K., 2004. A combined modeling and measurement technique for estimating windblown dust emissions at Owens (dry) Lake, California. J. Geophys. Res. Earth 109, F1.

Gillette, D.A., 1999. A qualitative geophysical explanation for "hot spot" dust emitting source regions. Contrib. Atmos. Phys. 72 (1), 67–77.

Gillies, J.A., Nickling, W.G., King, J., 2006. Aeolian sediment transport through large patches of roughness in the atmospheric inertial sublayer. J. Geophys. Res. Earth 111. http://dx.doi.org/10.1029/2005JF000434, F02006.

Gillies, J.A., Nickling, W.G., King, J., 2007. Shear stress partitioning in large patches of roughness in the atmospheric inertial sublayer. Bound. Lay. Meteorol. 122 (2), 367–396.

Goossens, D., Buck, B., 2009. Dust dynamics in off-road vehicle trails: Measurements on 16 arid soil types, Nevada, USA. J. Environ. Manage. 90 (11), 3458–3469.

Greeley, R., Gaddis, L., Lancaster, N., Dobrovolskis, A., Iversen, J.D., Rasmussen, K.R., Saunders, R.S., Van Zyl, J., Wall, S., Zebker, H., White, B.R., 1991. Assessment of aerodynamic roughness via airborne radar observations. Acta Mech. Supplement. 2, 77–88.

Hanna, S.R., Briggs, G.A., Hosker Jr., R.P., 1982. Handbook on Atmospheric Diffusion. Technical Information Center U.S. Dpeartment of Energy, pp. 20–21.

Hodge, R., Brasington, J., Richards, K., 2009. In situ characterization of grain-scale fluvial morphology using terrestrial laser scanning. Earth Surf. Proc. Land. 34 (7), 954–968.

Irwin, H.P.A.H., 1981. A simple omnidirectional sensor for wind-tunnel studies of pedestrian-level winds. J. Wind Eng. Ind. Aerodynam. 7 (3), 219–239.

Jester, W., Klik, A., 2005. Soil surface roughness measurement – methods, applicability, and surface representation. CATENA 64 (2–3), 174–192.

Kavouras, I.G., Etyemezian, V., Nikolich, G., Gillies, J.A., Sweeney, M., Young, M., Shafer, D., 2009. A new technique for characterizing the efficacy of fugitive dust suppressants. J. Air Waste Manage. Assoc. 59 (5), 603–612.

King, J., Etyemezian, V., Sweeney, M., Buck, B.J., Nikolich, G., 2011. Dust emission variability at the Salton Sea, California, USA. Aeolian Res. 3, 67–79.

Kirby, R.P., 1991. Measurement of surface-roughness in desert terrain by close range photgrammetry. Photogramm. Rec. 13 (78), 855–875.

Lane, S.N., James, T.D., Crowell, M.D., 2000. Application of digital photogrammetry to complex topography for geomorphological research. Photogramm. Rec. 16 (95), 793–821.

Lettau, H., 1969. Note on the aerodynamic roughness-parameter estimation on the basis of roughness-element description. J. Appl. Meteorol. 8, 828–832.

Lettau, K., Lettau, H., 1978. Experimental and micrometeorological field studies of dune migration. In: Lettau, K., Lettau, H. (Eds.), Exploring the World's Driest Climate, vol. 101. University of Wisconsin—Madison IES Rep., pp. 110–147.

Marshall, J.K., 1971. Drag measurements in roughness arrays of varying densities and distribution. Agr. Meteorol. 8, 269–292.

Nickling, W.G., Gillies, J.A., Brown, L., J. Trant, J., 2011. Direct Measurements of Potential Dust Emissions at the Williston Reservoir Using PI-SWERL and Modeling of Potential Dust Emissions. Final Report Prepared for British Columbia Hydro, Richmond, BC, February 2011.

Nield, J.M., King, J., Wiggs, G.F.S., Leyland, J., Bryant, R.G., Chiverrell, R.C., Darby, S.E., Eckardt, F.D., Thomas, D.S.G., Vircavs, L.H., Washington, R., 2013. Estimating aerodynamic roughness over complex surface terrain. J. Geophys. Res. Atmos. 118, 12948–12961.

Nikuradse, J., 1933. Strömungsgesetze in rauhen Rohren. Forschungsarbeiten auf dem Gebiete des Ingenieurwesens. VDI-Verlag, Berlin, p. 361.

Prandtl, L., 1925. Bericht über Untersuchungen zur ausgebildeten Turbulenz. Z. Angew Math. Mech. 5, 136–139.

Raupach, M.R., 1992. Drag and drag partition on rough surfaces. Bound.-Lay. Meteorol. 60, 375–395.

Raupach, M.R., Gillette, D.A., Leys, J.F., 1993. The effect of roughness elements on wind erosion threshold. J. Geophys. Res. 98 (D2), 3023–3029.

Raupach, M.R., Hughes, D.E., Cleugh, H.A., 2006. Momentum absorption in rough-wall boundary layers with sparse roughness elements in random and clustered distributions. Bound. Lay. Meteorol. 120, 201–218, 210.1007/s10546-10006-19058-10544.

Sankey, J.B., Glenn, N.F., Germino, M.J., Gironella, A.I.N., Thackray, G.D., 2010. Relationships of aeolian erosion and deposition with LiDAR-derived landscape surface roughness following wildfire. Geomorphology 119 (1–2), 135–145.

Sankey, J.B., Eitel, J.U.H., Glenn, N.F., Germino, M.J., Vierling, L.A., Lee, A., 2011. Quantifying relationships of burning, roughness, and potential dust emission with laser altimetry of soil surfaces at submeter scales. Geomorphology 135 (1–2), 181–190.

Schlichting, H., Gersten, K., 2000. Bound. Layer Theory, eighth ed. Springer-Verlag, Berlin, ISBN 3-540-66270-7.

Shao, Y., Yang, Y., 2008. A theory for drag partition over rough surfaces. J. Geophys. Res. Earth 113. http://dx.doi.org/10.1029/2007JF000791, F02S05.

Sweeney, M., Etyemezian, V., MacPherson, T., Nickling, W., Gillies, J.A., Nikolich, G., McDonald, E., 2008. Calibration of PI-SWERL with dust emission measurements from a straight-line wind tunnel. J. Geophys. Res. Earth 113 (F1). http://dx.doi.org/10.1029/2007JF000830, F01012.

Sweeney, M., McDonald, E.V., Etyemezian, V., 2011. Quantifying dust emissions from desert landforms. Geomorphology 135, 21–34.

Wooding, R.A., Bradley, E.F., Marshall, J.K., 1973. Drag due to regular arrays of roughness elements of varying geometry. Bound.-Lay. Meteorol. 5, 285–308.